

# X-ray Study of the Dark Matter Distribution in Clusters of Galaxies with Chandra

Haruyoshi KATAYAMA

*Japan Aerospace Exploration Agency, 2-1-1, Sengen, Tsukuba, Ibaragi 305-8505*

*hkatayam@oasis.tksc.jaxa.jp*

and

Kiyoshi HAYASHIDA

*Graduated School of Osaka University, 1-1, Machikaneyama, Toyonaka, Osaka 560-0043*

*hayasida@ess.sci.osaka-u.ac.jp*

(Received ; accepted )

## Abstract

We study the total gravitating mass distribution in the central region of 23 clusters of galaxies with *Chandra*. Using a new deprojection technique, we measure the temperature and gas density in the very central region of the clusters as a function of radius without assuming any particular models. Under the assumptions of hydrostatic equilibrium and spherical symmetry, we obtain the deprojected mass profiles of these clusters.

The mass profiles are nicely scalable with a characteristic radius ( $r_{200}$ ) and mass ( $M_{200}$ ) on the large scale of  $r > 0.1r_{200}$ . In contrast, the central ( $r < 0.1r_{200}$ ) mass profiles have a large scatter even after the scaling. The inner slope  $\alpha$  of the total mass density profile ( $\rho(r) \propto r^{-\alpha}$ ) is derived from the slope of the integrated mass profile. The values of the inner slope  $\alpha$  at the radius of  $0.02r_{200}$  ( $\alpha_0$ ) span a wide range from 0 to 1.2. For 6 out of 20 clusters,  $\alpha_0$  is lower than unity at a 90 % confidence level. CDM simulations predict that the inner slope  $\alpha$  is in the range  $1 < \alpha < 2$ , which is inconsistent with our results. We also found that the gas fraction near the center of a cluster has a negative correlation with  $\alpha_0$ . Our result suggests that the gas-rich clusters in the central region tend to have a flat core.

**Key words:** galaxies: clusters: general – cosmology: dark matter – X-rays: galaxies: clusters

## 1. Introduction

The Cold Dark Matter (CDM) model has become the standard paradigm for explaining observations of the large-scale structure of the universe. In the CDM model, dark matter consists of non-baryonic, collisionless, cold particle. The properties of dark matter density profiles in the CDM model have been investigated extensively through numerous N-body simulations. Navarro, Frenk, & White (1997) (hereafter NFW) claimed that the dark matter density profiles in the CDM model are reasonably approximated by a universal form with singular behavior in its central region. Several N-body simulations predict that the density of dark matter increases as a power law  $\rho(r) \propto r^{-\alpha}$ , with  $\alpha$  in the range of 1 to 2, in the central region (e.g.,  $\alpha = 1$  by NFW;  $\alpha = 1.5$  by Moore et al. (1998)). Measurements of the inner slope  $\alpha$  of dark matter density profiles offer a powerful test of the CDM model.

The observational efforts in this respect have been in the form of dynamical studies of low surface brightness and dwarf galaxies. The observations obtained in those studies suggest the presence of a relatively flat core:  $0 < \alpha < 1$  (e.g., Firmani et al. (2001)). Gravitational lensing has made some observational constraints available at the scale of galaxy clusters. For instance, Sand, Treu, & Ellis (2002) showed that steep inner slopes ( $\alpha > 1$ ) are ruled out at better than 99 %, for the lensing cluster MS2137-23. Although gravitational lensing studies provide a unique and important probe of dark matter profiles, they generally can be applied only to a limited sample of clusters that satisfy a specific lensing condition. X-ray observations of the density and temperature of a hot intracluster medium (ICM), on the other hand, probe the mass of a cluster of galaxies under the assumption of hydrostatic equilibrium. This could be a powerful tool to investigate dark matter profiles in the central regions of clusters. However, for previous X-ray satellites, such as *ROSAT* and *ASCA*, the detailed study of ICM temperature and density profiles at small scales has been difficult because of limitations on the performance of imaging or spectroscopic instruments. The high spatial resolution imaging spectroscopy of *Chandra* enables the measurement of mass profiles in the very central regions of clusters of galaxies. Several groups have obtained X-ray constraints on the dark matter profiles of some clusters. These results are apparently consistent with the CDM model (e.g., David et al. (2001), and Arabadjis, Bautz, & Garmire (2002)). However, Ettori, Fabian, Allen, & Johnstone (2002) showed that the mass profile of A1795 flattens within 100 kpc. Systematic studies are thus required for a large sample of clusters. In this paper, we systematically study the mass profiles of 23 clusters of galaxies.

We assume  $\Omega_m = 1$ ,  $\Omega_\lambda = 0$ , and  $H_0 = 50 \text{ km s}^{-1} \text{ Mpc}^{-1}$  throughout this paper. Unless otherwise noted, all errors are  $1\sigma$  (68.3 %) confidence intervals.

## 2. Sample and Analysis

We selected our sample from *Chandra* archival data of galaxy clusters. To obtain spatially resolved spectra, we restricted the observations to those in which ACIS were employed without gratings. By the end of September 2002, the archive contained observation data for about 150 clusters ( $\sim 200$  pointings) that met this criterion.

We applied the following criteria for further selection of the data in order to meet our main concern, investigation of the central mass profiles of galaxy clusters. First, clusters must be bright enough to provide spatially resolved spectra with good statistics. For this we referred to the catalog of Reiprich & Böhringer (2002), which consists of 106 bright clusters compiled from several catalogs based on the *ROSAT* All-Sky X-ray Survey (Voges et al. (1999)). The minimum X-ray flux among the Reiprich samples is  $0.234 \times 10^{-11}$  ergs s $^{-1}$  cm $^{-2}$  (0.1–2.4 keV). This is bright enough for our analysis under typical observational conditions. Among the 106 clusters in Reiprich sample, 43 clusters are included in the *Chandra* data archive. Secondly, clusters should be spherically symmetric as our deprojection analysis assumes the spherical symmetry. We thus excluded merging clusters like A754 (Henriksen & Markevitch (1996)). Although this second criterion is somewhat ambiguous, we will examine how this spherical symmetry assumption affects the final result in Section 5. The last criterion is that the X-ray emission from the outer region of a cluster must be covered by the detectors used in the observations. This is because the deprojection analysis depends on accurate measurement of temperatures and densities of the outer regions of clusters. Data for 20 clusters met all of these criteria. We also employed three distant clusters, A1835, A963, and ZW3146, that are bright and spherically symmetric but that are not included in Reiprich & Böhringer (2002).

The observation log and the properties of each cluster are summarized in Table 1 and Table 2, respectively. The redshifts of the 23 sample clusters range from 0.0110 to 0.2906, with a median of 0.0852.

Data reduction and analysis were performed with the *Chandra* Interactive Analysis of Observations package, CIAO-2.2, with calibration database CALDB-2.12, as provided by the *Chandra* X-ray Center (CXC). We started the reduction from the standard level 2 event files archived at CXC, which are the products of the pipeline processing. We adopted the standard reduction scheme by following the CIAO threads<sup>1</sup>.

To remove the flare events, we performed lightcurve screening using the CIAO task *lc\_clean*. We made a background lightcurve, a time history of the event rate taken from a source-free region on the detector, with a time bin size of 259.28 s using the CIAO task *lightcurve*. In order to exclude flare events, we discarded the data taken at the time the count rate deviates from the mean by  $\pm 3\sigma$ , where the mean value is defined during the quiescent period. Point source detection was performed with the CIAO wavelet source detection routine *wavdetect* with

---

<sup>1</sup> <http://asc.harvard.edu/ciao/threads>

a significance parameter  $10^{-6}$ . We made a 0.3–10 keV image binned by using a bin size of about  $2 \times 2''$  ( $4 \times 4$  pixels). The area around the detected point sources was excluded in the following analysis. In order to estimate the background level to be subtracted from the X-ray spectra and images, we applied the blank-sky data compiled by Markevitch (2001)<sup>2</sup> as background data. These background data are event files made with the same lightcurve screening process of the cluster data.

The spectra were extracted in the concentric annuli centered on the X-ray peak with different widths to ensure similar statistics in the background-subtracted spectra. The X-ray peak was determined with the X-ray images from which point sources were removed. We examine what the appropriate setup is for the width of the annuli, or equivalently, the statistics of each spectrum, using a simulation. From this simulation, we found that the lower photon counts or the more annulus result in the larger systematic errors in the temperature profile as shown in Arabadjis, Bautz, & Garmire (2002). In order to suppress the systematic errors in the temperature profile, we restricted the photon count per each annulus and the number of annuli, as follows: (1) The photon count per each annulus must be at least  $1 \times 10^4$ , and (2) The number of annuli  $N$  must be  $5 \leq N \leq 10$ . The radius of the outermost annulus was determined to cover the  $4\text{-}\sigma$  background level of the *ROSAT* PSPC image. The average of the outermost radius is about 720 kpc. The background spectra were extracted from the background data with the same regions on the detector. Redistribution Matrix Files (RMF) and Auxiliary Response Files (ARF) were made using the CIAO tasks of *mkrmf* and *mkwarf*. These tasks make a weighted RMF and a weighted ARF for the spectral analysis based on a  $32 \times 32$  pixel grid of calibration files. This is because the RMF and ARF vary with detector location. To compensate for the degradation in low-energy efficiency, we used the tool *corrarf* provided by CXC. The *corrarf* corrects the ARF according to the observation date.

### 2.1. Deprojection Analysis

To determine the deprojected temperature and gas density profiles, we applied a new deprojection technique developed by Arabadjis, Bautz, & Garmire (2002). We here briefly summarize this technique (see also Arabadjis, Bautz, & Garmire (2002) and Katayama (2003)).

A Schematic view of the deprojection analysis is shown in Figure 1 (Left). In this example, we extract spectra from  $N$  concentric annular regions. The projected luminosity  $S_j$  in a given energy band on the  $j$ th annulus is expressed by the integration of emissivities along the line of sight. The relationship between  $S_j$  and the volume emissivity  $e_i$  of the  $i$ th spherical shell is expressed as

$$S_j = \sum_{i=j}^N V_{ij} e_i. \quad (1)$$

where  $V_{ij}$  is the volume of the  $i$ th spherical shell intersected by a cylindrical shell whose radius

<sup>2</sup> <http://cx.c.harvard.edu/contrib/maxim/bg/index.html>

equals the  $j$ th projected annulus. Note that we have to make sure, or make the assumption that, X-ray emission is negligible outside of the outermost annulus.  $V_{ij}$  is geometrically calculated as

$$\begin{aligned} V_{ij} &= \frac{4}{3}\pi[(r_{i+1}^2 - b_j^2)^{3/2} - (r_{i+1}^2 - b_{j+1}^2)^{3/2} - (r_i^2 - b_j^2)^{3/2} + (r_i^2 - b_{j+1}^2)^{3/2}] \quad (i \geq j) \\ &= 0 \quad (i < j), \end{aligned} \quad (2)$$

where  $r_i$  and  $r_{i+1}$  are the inner and outer radii of the  $i$ th spherical shell, and  $b_j$  and  $b_{j+1}$  are the inner and outer radii of the  $j$ th annulus, which equal  $r_j$  and  $r_{j+1}$ , respectively. Since Equation 1 can also be written for all annuli, these are written as

$$\mathbf{S} = \mathbf{V} \cdot \mathbf{e}. \quad (3)$$

Since  $\mathbf{V}$  is a triangle matrix, we can obtain the  $\mathbf{e}$  by solving the inverse matrix  $\mathbf{V}^{-1}$ .

In most previous deprojection analyses, only X-ray spatial information was utilized and an additional assumption on the temperature profile  $kT(r)$  or the potential profile  $\phi(r)$  was necessary. Even when both types of information are available, some authors assume the potential profile  $\phi(r)$ , or equivalently, the gravitational mass density profile  $\rho(r)$ , beforehand. However, the method by Arabadjis, Bautz, & Garmire (2002) does not make such assumptions. We first make a trial model for volume emissivity  $e_i$  at each spherical radius, which is a function of gas temperature  $kT_i$ , gas density  $n_{g,i}$  and gas abundance  $Z_i$  when we employ an X-ray emissivity model of thin thermal plasma. We adopted the MEKAL (Mewe, Gronenschild, & van den Oord 1985; Mewe, Lemen, & van den Oord 1986; Kaastra & Mewe 1993; Liedahl, Osterheld, & Goldstein 1995) model in the XSPEC data analysis package for our X-ray emissivity model, in which normalization  $K_i$  is used instead of gas density  $n_{g,i}$ . Therefore, the number of free parameters to be determined is  $3 \times N$  except for an additional free parameter for the interstellar absorption  $N_{\text{H}}$ . We can examine how this trial model fits the set of spectra by  $\chi^2$  value, and we can improve the fit by changing the parameter values  $kT_i$ ,  $n_{g,i}$ , and  $N_{\text{H}}$ . This procedure is done with the XSPEC data analysis package as a simultaneous spectral fitting of  $N$  spectra. For some clusters, the interstellar absorption was poorly constrained. In such case, we fixed the absorption column to the Galactic value. We show the sample of the fitting result in Figure 1 (Right).

### 3. Temperature and Gas Density Profiles

We determined the temperature and gas (electron) density profiles of all sample clusters. Figure 2 shows the temperature, gas density, pressure profiles of A2597. The pressure profiles are simply derived from the temperature and gas density with the equation of the state of ideal gas:  $P = n_e kT$ . We attempted to model the temperature and density profiles with analytic functions. Note that the total mass profile can be calculated without employing such models, as shown in the next section. However, we investigated for another way to obtain the total mass profile, to which end such models are employed. We fitted the temperature profile with

exponential + constant model given by

$$T(r) = T_0 + T_1 \exp(-r/r_T). \quad (4)$$

The fitting results are summarized in Table 3. Three parameters in the exponential + constant model were determined by the  $\chi^2$  fitting, but their error estimation was not trivial when the fitting was unacceptable. These large reduced  $\chi^2$  values are likely to be due to local fluctuations in the intrinsic temperature profiles or to unknown systematic errors in our analysis procedure. Note that we integrate the above model functions within one radius bin to obtain each model point. Thus, a coarse sampling is not the cause of the large  $\chi^2$  values. In order to estimate conservative errors for the parameters, we assigned a systematic error to each data point in the temperature profile. The systematic error of the temperature is assumed to be the constant fraction of the measured temperature for all the data points, where the fraction is determined so as to obtain the reduced  $\chi^2$  of unity in each temperature profile. Note that the total error is calculated to be the square root of the quadratic sum of the statistical and systematic errors. For some clusters, the original (i.e., before assignment of the systematic error) reduced  $\chi^2$  is small enough to accept the fit. We assigned the systematic error only for the clusters for which the original fitting was rejected by the  $\chi^2$  test with a significance level less than 1 %. We also fitted the gas density profile with NFW gas density model given by

$$n_g(r) = n_{e0} \exp\left[-B\left(1 - \frac{\ln(1 + (r/r_s))}{(r/r_s)}\right)\right] \quad (5)$$

(Makino, Sasaki, & Suto 1998). The fitting results are summarized in Table 4. As was the case for the temperature profiles, we adopted the systematic error for all the clusters.

#### 4. Mass Profiles

Under the assumptions of hydrostatic equilibrium and spherical symmetry, we can obtain the total gravitating mass profile as a function of radius using

$$\begin{aligned} \frac{dP_g}{dr} &= -\mu n_g m_p \frac{d\phi}{dr} \\ &= -\mu n_g m_p \frac{GM(< r)}{r^2}. \end{aligned} \quad (6)$$

We derived this mass profile by two different methods in order to check its consistency. The first method employs the temperature and density profile models obtained in Section 3. Substituting Equation 4 and Equation 5 for Equation 6, we obtain the mass profile in an analytic form. The second method does not employ the temperature and density profile models. Instead, the mass profile is derived by approximating Equation 6 as simple differences:

$$M(< r) \sim -\frac{1}{\mu n_g(r) m_p} \frac{r^2}{G} \frac{\Delta P(r)}{\Delta r}. \quad (7)$$

We calculated  $\Delta P(r)/\Delta r$  as

$$\frac{\Delta P(r)}{\Delta r} = \frac{P_{i+1} - P_i}{r_{i+1} - r_i} \quad (8)$$

where  $P_i$  and  $r_i$  are the pressure and radius of the  $i$ th shell. The radius  $r$  and gas density  $n_g(r)$  are given by  $r = (r_{i+1} + r_i)/2$  and  $n_g(r) = (n_{ei+1} + n_{ei})/2$ , respectively.

Results of these two methods are compared in Figure 3 for A2597. The plots also show the  $1\sigma$  confidence levels for the analytic mass profile, which is derived by considering the errors of the parameters describing the temperature and density profile models. The mass profiles derived by the two different methods were consistent in most of the cases. In the case that the pressure of the outer shell is larger than that of the inner shell ( $P_{i+1} > P_i$ ), the mass profile shows the negative value at that point :  $M < 0$ . This is likely caused by the local temperature fluctuation intrinsic at some radius of the clusters or by systematic errors in our analysis. We excluded these unphysical points in the analysis, though such points are only seen in NGC5044 and Centaurs. Of the two derivation methods, the first one using the modeled temperature and density profiles is easy to handle, but it involves sacrificing one important point of the deprojection analysis; i.e., no reliance on any particular profile models. On the other hand, the second method is more straightforward, but it suffers large error owing to local fluctuations in the temperature and density profiles.

#### 4.1. *Scaling of Mass Profiles*

In Figure 4, we show the analytic mass profiles of 23 sample clusters in one plot, illustrating the scatters among them. CDM simulations predict that the density profiles of dark matter are universal in form across a wide range of mass scales (Navarro, Frenk, & White 1995; Navarro, Frenk, & White 1996). We scaled our analytic mass profiles with  $r_{200}$  and  $M_{200}$ , where  $r_{200}$  is the radius within which the mean halo density is 200 times the critical density of the universe, and  $M_{200}$  is the total mass enclosed within  $r_{200}$ . As shown by Navarro, Frenk, & White (1995), and Navarro, Frenk, & White (1996), clusters of different mass are expected to show similar structures when scaled to such a characteristic radius and mass. For the calculation of  $r_{200}$ , we used the relation obtained from the numerical simulation by Evrard, Metzler, & Navarro (1996):

$$r_{200} = 3.690 (T/10\text{keV})^{0.5} (1+z)^{-1.5} \text{ [Mpc]}, \quad (9)$$

where  $T$  is the spatially averaged temperature, and  $z$  is the redshift.  $M_{200}$  is calculated by

$$M_{200} = \frac{4}{3}\pi(200\rho_{\text{crit}}(z)) r_{200}^3. \quad (10)$$

where  $\rho_{\text{crit}}(z) = 3H(z)^2/8\pi G$  is the critical density of the universe at a redshift  $z$ . We show the scaled mass profiles in Figure 5. On a large scale ( $r > 0.1r_{200}$ ), the scaled mass profiles agree with each other better than did the original mass profiles, except in the case of one deviant profile of A401. This findings suggest that the mass profiles have a similar form on a large scale; in other words, the scaling with  $r_{200}$  and  $M_{200}$  is effective at least on this scale. The standard deviation of the mass profiles is 41 % at 200 kpc for the original mass profiles, and that for

the scaled profiles is 21 % at  $0.1r_{200}$ , which corresponds to about 160–300 kpc. In contrast, the standard deviations on the small scale ( $r < 0.1r_{200}$ ) are not significantly different: 55 % at 20 kpc for the original mass profiles, and 60 % at  $0.01r_{200}$  for the scaled mass profiles.

When the density profile of dark matter is described with the power-law expression  $\rho(r) = \rho_0(r/r_0)^{-\alpha}$ , the mass integrated over the volume is described by

$$M(< r) = \int_0^r 4\pi\rho(r')r'^2dr' = \frac{4\pi\rho_0r_0^3}{3-\alpha}\left(\frac{r}{r_0}\right)^{3-\alpha}. \quad (11)$$

Therefore, the smaller the value of  $\alpha$  is ( $\alpha \rightarrow 0$ ), the steeper the mass profile is. We overlaid the  $M \propto r^{1.5}$  ( $\alpha = 1.5$ ),  $M \propto r^2$  ( $\alpha = 1$ ) and  $M \propto r^3$  ( $\alpha = 0$ ) lines on the scaled mass profiles in Figure 5. It was found that the slope  $\alpha$  was in the range of 0 to 1.5, and it was flatter (smaller) on the small scale. The slope  $\alpha$  at the cluster center is quantitatively examined in Section 4.2

#### 4.2. Inner Slope of Dark Matter Distribution

The shape of the dark matter distribution near the center of a cluster is sensitive to the theoretical models adopted. In this section, we focus on the observed shape of the total mass distribution in terms of the slope of the density profile at the inner part of a cluster. The inner slope of the density profile is obtained by fitting the total mass profile we obtained with a model mass profile calculated from an assumed density profile. Although we employed the King and NFW profiles as density profile models in the previous section, a more generalized form is used in this section. That form was

$$\rho(r) = \frac{\rho_0}{(r/r_s)^\alpha(1 + (r/r_s))^{(3-\alpha)}}, \quad (12)$$

where  $\rho_0$  is the central density,  $r_s$  is its scale radius, and  $\alpha$  is the asymptotic slope of the profile at small radii. This form of density profile requires numerical integration to derive the integrated mass profile. The asymptotic slope  $\alpha$  in Equation 12 can be used as the inner slope. However, it was found that the asymptotic slope  $\alpha$  and the scale radius  $r_s$  are coupled strongly, and therefore difficult to determine independently. Thus, we focus on the slope of the density profile at a finite radius and used it as the inner slope. The slope at a radius  $r_0$ ,  $\alpha_0(r_0)$  is given by

$$\alpha_0(r_0) \equiv -\frac{d\ln\rho(r)}{d\ln r} \Big|_{r=r_0}. \quad (13)$$

Using Equation 12, we get

$$\alpha_0(r_0) = \frac{(\alpha + (r_0/r_s))}{(1 + (r_0/r_s))}. \quad (14)$$

We employ  $\alpha_0(r_0)$  instead of  $\alpha$ , in addition to  $\rho_0$  and  $r_s$ , as a free parameter of the fitting. We fixed  $r_0$  to  $0.02r_{200}$ , which corresponds to about 40 kpc. The choice of  $r_0$  is not trivial, but we fix this value so that the radius is appropriate for a comparison of the theoretical models and is covered by observed data points in the mass profile. Nevertheless, A401, A644, and A963, due to a lack of data points within  $0.02r_{200}$ , were discarded from the following analysis. Since the



mass profiles of some clusters are nearly power-law, we could not determine  $r_s$ . In such case, we fixed  $r_s$  to 1 Mpc, which is the radius that there is no data for all clusters.

The results of the fitting are summarized in Table 5, and the best-fit values and errors of the inner slope  $\alpha_0(r_0)$  are plotted in Figure 6. We also show the total mass profiles with the best-fit models for the general form of the density profile in Figure 7. The inner slope  $\alpha_0$  spans a wide range with  $0 \leq \alpha_0 \leq 2.3$ . We found that the 90% upper bound of  $\alpha$  was lower than unity for 6/20 ( $\sim 41$  %) clusters (A2052, A2597, A478, PKS0745-191, ZW3146, and 2A0335+096), suggesting that the dark matter distribution in a significant fraction of clusters was flatter than that in CDM halo models such as the NFW profile or the Moore profile.

## 5. Examination of the Systematic Effects

We have demonstrated that the inner slope  $\alpha_0$  shows a large scatter and is less than unity for 30% of the clusters in our sample. Before discussing these results in greater detail, we would like to address their validity and the systematic effects that may affect the measured inner slope from various points of view.

### 5.1. Center Position

We can define three types of positions as the center of a cluster: (1) the X-ray emission peak of cluster hot gas; (2) the X-ray centroid; and (3) the position of the Brightest Cluster Galaxy (BCG). We chose the X-ray emission peak as the center of the annuli to extract spectra. Since these three positions are slightly different, the selection of the center position may affect our results.

We first examined the position of the BCG in our sample clusters. The BCG is defined as the brightest galaxies among the member galaxies of a cluster. Since the BCGs are usually located at the center of a cluster and have velocities very near the mean velocity of galaxies in the cluster, they are considered to sit at the bottom of the cluster gravitational potential well. The positions of BCGs were taken from the NASA/IPAC Extragalactic Database (NED)<sup>3</sup>. We calculated the offset between the X-ray peak and the position of the BCG. When the offset was larger than or comparable to the radius of the innermost annulus, the temperature or density profiles will be affected by the selection of the center. In Figure 8, the offsets of the BCG are plotted against the radii of the innermost annulus. The offsets of the BCG are smaller than the radius of the innermost annulus ( $\sim 30$  % at the maximum) except for 2A0335, suggesting that the difference in cluster center between these two definitions did not affect our results significantly.

We next examined the offset between the X-ray peak and the X-ray centroid. To derive the X-ray centroid, we used the X-ray images in which point sources were removed. We replaced each embedded source with the local diffuse X-ray emission surrounding the source by using

---

<sup>3</sup> <http://nedwww.ipac.caltech.edu>

the CIAO task *dmfilth*. This task replaces the counts within the source regions with the values sampled from the background regions. As the ACIS CCDs do not cover the entire X-ray emission for most clusters. We thus define the X-ray centroid within a circular region that is centered on the X-ray peak and has a radius that is tangent to the detector edge. The offsets between the X-ray peak and the X-ray centroid are plotted against the radii of the innermost annulus in Figure 9. The offsets of the X-ray centroid are slightly larger than the offsets of the BCG but are smaller than the radii of the innermost annulus. The offset is at most 74 % (for A644) of the radius of the innermost annulus, suggesting that the difference in these definitions of a cluster center does not significantly affect the results.

## 5.2. Spherical Symmetry

When we selected our sample, we excluded some clusters which are not spherical symmetric in appearance. To quantify the spherical symmetry, we measured the ellipticity ( $\epsilon$ ) and the position angle ( $PA$ ) from the projected X-ray image. We used an iterative moment technique derived from the treatment of the dispersion ellipse of the bivariate normal frequency function of position vectors used by Carter & Metcalfe (1980). We first calculated the moments of the observed X-ray images. From an image of  $P$  pixels having  $n_i$  counts in pixel  $i$ , we computed the moment

$$\mu_{mn} = \frac{1}{N} \sum_{i=1}^P n_i (x_i - \bar{x})^m (y_i - \bar{y})^n \quad (m, n \leq 2), \quad (15)$$

where  $N = \sum_{i=1}^P n_i$ , and  $(\bar{x}, \bar{y})$  is the centroid. Then ellipticity  $\epsilon$  is

$$\epsilon = 1 - \frac{\Lambda_-}{\Lambda_+}, \quad (16)$$

and the position angle of the major axis measured north through east in celestial coordinates is

$$PA = \tan^{-1} \left( \frac{\mu_{11}}{\Lambda_+^2 - \mu_{02}} \right) + \frac{\pi}{2}, \quad (17)$$

where  $\Lambda_{\pm}$  ( $\Lambda_+ \geq \Lambda_-$ ) are the positive roots of the quadratic equation

$$\begin{vmatrix} \mu_{20} - \Lambda^2 & \mu_{11} \\ \mu_{11} & \mu_{02} - \Lambda^2 \end{vmatrix} = 0. \quad (18)$$

As in the case of the determination of the X-ray centroids, we used the X-ray images from which point sources were removed and replaced with local diffuse X-ray emission surrounding the source. We also employed the *ROSAT* images to determine the ellipticities and position angles in outer regions of clusters. From the *ROSAT* image, the point sources were removed but the holes were not replaced with the background. We consider that if the ellipticity of a cluster affects the inner slope  $\alpha_0$ , the ellipticity  $\epsilon$  and the inner slope  $\alpha_0$  will show some kind of relation. However, the plot in Figure 10 shows no correlation between the ellipticity  $\epsilon$  at  $r = 0.05r_{200}$  and the inner slope  $\alpha_0$  (the correlation coefficient is -0.31). We therefore conclude

that there was no evidence that deviation from spherical symmetry affects the results on the inner slope  $\alpha_0$ , although we cannot obtain no evidence regarding symmetry along the line of sight.

### 5.3. Central Structure

Recent *Chandra* observations have revealed remarkable structures in the hot gas of the central region of some cooling flow clusters. These structures may have observably affected the temperature and gas density in our measurement. Furthermore, if these structures indicate a break of hydrostatic equilibrium, they may systematically have affected the mass profile we obtained. For 10 clusters in our sample, the presence of central X-ray structures such as a cavity, hole, or plume has been reported with *Chandra* observations in the literature (Table 6).

In Figure 11, we show the inner slope  $\alpha_0$  again, indicating 10 clusters for which the central structure has been found by open circles. It is found that the three clusters in which  $\alpha_0$  is as steep as 2 have central structures, and the range of  $\alpha_0$  becomes narrower if we neglect them. However, the distribution of  $\alpha_0$  from 0 to 1.2 is similar for clusters with and those without central structures, though this is difficult to conclude quantitatively. Note that some of the central structures, such as those in A133, A2597, and MKW3S are small enough to be removed from the analysis. In order to evaluate the observational effect of these structures, we removed the region of these structures from those clusters and confirmed that the mass profiles were not significantly affected.

## 6. Relations between Inner Slope and Other Observational Parameters

As shown in Section 4.2, the inner slope  $\alpha_0$  of the density profiles spans a wider range than that estimated from their errors. Even if we neglect the three clusters in which central structures might affect the results,  $\alpha_0$  ranges from 0 to 1.2 and spreads toward a flatter side than expected based on CDM simulations. If this spread of the distribution is intrinsic, what is it that determines the inner slope of the density profile? In this section, we explore observational parameters that primarily determine the inner slope  $\alpha_0$ , by examining their correlations.

### 6.1. Redshift vs. $\alpha_0$

We first show the relation between the redshift and the inner slope  $\alpha_0$  in Figure 12. The correlation coefficient is -0.25 for this relation. Note that the range of redshifts in our sample may not be sufficient to investigate the effect of cosmological evolution.

### 6.2. Temperature vs. $\alpha_0$

We plot the spatially averaged temperature  $kT_{\text{average}}$  against the inner slope  $\alpha_0$  in Figure 13. The correlation coefficient is 0.01. Simple arguments based on virial theorem suggest that the mass of a cluster is simply related to the cluster temperature as  $M \propto T^{3/2}$ . This relation implies that the inner slope  $\alpha_0$  is not related to the scale of the cluster.

### 6.3. Gas Fraction vs. $\alpha_0$

We next investigated the relation between the gas fraction and the inner slope  $\alpha_0$ . The gas fraction is the ratio of the hot gas mass to the total mass, and is defined as a function of radius. The integrated gas mass profile  $M_{\text{gas}}(< r)$  is given by

$$\begin{aligned} M_{\text{gas}}(< r) &= \int_0^r 4\pi r'^2 \rho_{\text{gas}}(r) dr' \\ &= 4\pi \mu m_p \int_0^r 4\pi r'^2 n_{\text{gas}}(r) dr', \end{aligned} \quad (19)$$

where  $n_{\text{gas}}(r)$  is the total number density of electrons and ions,  $\mu(=0.6)$  is the mean molecular weight, and  $m_p$  is the proton mass. The gas fraction is defined as

$$f_{\text{gas}}(r) \equiv \frac{M_{\text{gas}}(< r)}{M(< r)}. \quad (20)$$

In Figure 14, we present the profiles of total mass, gas mass, and gas fraction for 23 sample clusters. It was found that the gas fraction increases toward the center for some clusters. In Figure 15, the gas fractions at the radius of  $r = 0.05r_{200}$  are plotted against the inner slope  $\alpha_0$ . A negative correlation was observed with the correlation coefficient of  $-0.51$ , for which case, at a significance level of about 3%, the hypothesis of no correlation is rejected. This correlation might be a kind of artifact in the analysis, since we derive both the total mass profile and the gas mass profile from the same gas density profile and gas temperature profile. However, it is unlikely that the observed correlation is due to correlated errors between the two parameters, considering the size of the errors.

In order to examine this correlation is artifact or not, we took  $M_{200}$ , which is determined solely from the gas temperature and redshift, instead of the integrated mass profile. We redefined the gas fraction as

$$f'_{\text{gas}}(r) \equiv \frac{M_{\text{gas}}(< r)}{M_{200}}. \quad (21)$$

We plot  $f'_{\text{gas}}$  at the radius of  $r = 0.05r_{200}$  against the inner slope  $\alpha_0$  in Figure 16. Although the correlation coefficient of  $-0.40$  is smaller than that for  $f_{\text{gas}}$ , the no correlation hypothesis is rejected at a significance level of less than 10%.

Correlations between the inner slope  $\alpha_0$  and the gas fraction according indicate that gas-rich clusters in the central region tend to have a flat core:  $\alpha < 1$ .

## 7. Summary and Discussion

We have analyzed the *Chandra* data of 23 clusters of galaxies in order to investigate central mass distribution. The high spatial resolution imaging spectroscopy of *Chandra* and a new deprojection technique enable us to measure the temperatures and gas densities in the very central region of sample clusters without assuming any particular models. Under the assumptions of hydrostatic equilibrium and spherical symmetry, we obtained the deprojected

mass profiles. Our major results are as follows.

1. The mass profiles scaled with  $r_{200}$  and  $M_{200}$  agree each other on the large scale  $r > 0.1r_{200}$ . In contrast, the central ( $r < 0.1r_{200}$ ) mass profiles show a large scatter.
2. The inner slope  $\alpha_0$  of the density profile was derived by fitting the mass profile with a general form of dark matter density profile for 20 clusters. The values of  $\alpha_0$  span a wide range (from 0 to 2.3). For 6 out of 20 clusters,  $\alpha_0$  are lower than unity at a 90 % confidence level.
3. We investigated several features that might influence the results of the inner slope, including center position, ellipticity, and central structure of a cluster. We found that the systematic effects of these features are not significant except in the case of the central structure, which may broaden the distribution of the inner slope  $\alpha_0$ . However, even if we excluded the clusters in which central structures were seen, the inner slope  $\alpha_0$  distributes widely in the range from 0 to 1.2.
4. We examined the relationships between the inner slope  $\alpha_0$  and other observational parameters. Although redshift, averaged temperature, and variation in the temperature profile are not correlated with the inner slope  $\alpha_0$ , gas fraction near the center of a cluster has a negative correlation with  $\alpha_0$ .

CDM simulations predict that the inner slope  $\alpha$  is in the range  $1 < \alpha < 2$ . Therefore, our results are inconsistent with the CDM simulations. Our observations provide flatter slopes, at least for some clusters, than those expected from the CDM simulations. This is true even if we neglect the clusters showing central structures ( $0 < \alpha_0 < 1.2$ ).

A similar claim has been presented by authors who are investigating the rotation curve of galaxies and clusters. Firmani et al. (2001) examined the observed rotation curves of dwarf and low surface brightness (LSB) galaxies, and two clusters of galaxies, and found that all of those objects have soft cores:  $\alpha < 1$ . Swaters, Madore, van den Bosch, & Balcells (2003) observed the rotation curve of 15 dwarf and LSB galaxies and found inner slopes in the range of  $0 \lesssim \alpha \lesssim 1$  in the majority. This inconsistency between observations and simulations in terms of the dark matter distribution at the center of galaxies or clusters is called the core problem. Our results indicate that the core problem exists in a significant fraction of clusters observed through X-ray observations.

We also found a negative correlation between the inner slope and the gas fraction. In the central region of clusters, the baryonic components such as hot gas and stars in a galaxy are not negligible. These baryonic components are usually considered to follow the gravitational potential, which is predominantly determined by dark matter distribution. However, our results imply that these baryonic components affect the dark matter distribution in the central region of some clusters.

El-Zant, Shlosman, & Hoffman (2001) argued that the core problem can be resolved within the framework of the standard CDM model by considering the dynamical friction (DF)

between dark matter and gas. El-zant et al. assumed that the gas is not initially smoothly distributed but is, rather, concentrated in clumps. Such gas clumps move through smooth dark matter particles, lose energy to the central dark halo, and heat it up. This leads to the puffing up of the central regions and to the flattening of the density profile. Monte Carlo simulation by El-zant et al. successfully reproduced the observed flat density profile. In the DF model, the baryonic (gas) component is more centrally concentrated than dark matter, because gas gives its energy to dark matter and shrinks toward the center. So this model accounts for our observational result that gas rich clusters in the central region tend to have a flat core. Note that another numerical simulations including baryonic components show the cooling baryons adiabatically compress the dark matter and make a steeper central density profile (e.g., Blumenthal, Faber, Flores, & Primack 1986). However, this result is not consistent with our results because the gas rich cluster in the central region is expected to have steeper profile if the cooling baryons adiabatically compress the dark matter.

Although the DF model is one of many interpretations proposed to account for the core problem, our results indicate that the numerical simulation need to reconsider the treatment of the baryonic components in galaxies or galaxy clusters.

We thank all the staff members involved in the *Chandra* project. We acknowledge Jone Arabadjis and Mark Bautz for their support on the deprojection technique and their useful comments.

**Table 1.** Observation log of the sample clusters.

ID	Cluster	Obs. ID	Ra (deg) <sup>a</sup>	Dec (deg) <sup>a</sup>	Observation date	Exp. (ks)	Screened <sup>b</sup> Exp. (ks)	ACIS <sup>c</sup> chip
1	A1060	2220	159.073	-27.569	2001-06-04 04:43:23	31.9	30.0	I
2	A133	2203	15.689	-21.882	2000-10-13 22:27:02	35.5	34.5	S
3	A1795	493	207.205	26.608	2000-03-21 07:54:49	19.6	19.6	S
		3666	207.204	26.576	2002-06-10 16:21:19	14.4	13.8	S
		494	207.236	26.607	1999-12-20 05:00:57	19.5	17.6	S
4	A1835	495	210.272	2.895	1999-12-11 16:48:33	19.5	19.5	S
		496	210.222	2.867	2000-04-29 06:55:44	10.7	10.7	S
5	A2029	891	227.725	5.764	2000-04-12 06:38:56	19.8	19.8	S
6	A2052	890	229.182	7.012	2000-09-03 06:01:22	36.8	36.8	S
7	A2199	498	247.188	39.553	1999-12-11 10:47:37	18.9	18.9	S
		497	247.135	39.560	2000-05-13 17:36:15	19.5	17.9	S
8	A2204	499	248.185	5.557	2000-07-29 02:49:42	10.1	10.1	S
9	A2597	922	351.337	-12.135	2000-07-28 05:13:47	39.4	25.1	S
10	A401	518	44.727	13.579	1999-09-17 21:35:26	18.0	18.0	I
		2309	44.732	13.461	2000-11-03 19:10:36	11.6	11.6	I
11	A478	1669	63.362	10.436	2001-01-27 03:28:03	42.4	42.4	I
12	A644	2211	124.329	-7.543	2001-03-26 00:27:49	29.7	29.2	S
13	A85	904	10.442	-9.374	2000-08-19 07:06:52	38.4	38.4	I
14	A963	903	154.284	39.063	2000-10-11 00:01:18	36.3	36.3	S
15	AWM7	908	43.665	41.664	2000-08-19 18:30:01	47.9	47.9	I
16	Centaurus	504	192.207	-41.334	2000-05-22 00:33:17	31.7	28.8	S
		505	192.199	-41.334	2000-06-08 00:51:50	10.0	10.0	S
17	Hydra A	575	139.527	-12.091	1999-10-30 07:29:02	23.8	23.8	I
		576	139.527	-12.091	1999-11-02 11:31:54	19.5	19.5	S
18	MKW3S	900	230.488	7.757	2000-04-03 12:26:13	57.3	57.3	I
19	NGC5044	798	198.859	-16.378	2000-03-19 15:42:42	20.5	19.8	S
20	PKS0745-191	2427	116.860	-19.306	2001-06-16 05:32:52	17.9	17.9	S
		508	116.870	-19.277	2000-08-28 22:15:31	28.0	4.6	S
21	Sersic159-03	1668	348.515	-42.713	2001-08-13 16:41:20	9.9	9.9	S
22	ZW3146	909	155.905	4.166	2000-05-10 03:20:25	46.0	46.0	I
23	2A0335+096	919	54.666	10.008	2000-09-06 00:03:13	19.7	14.1	S

<sup>a</sup> Nominal pointing position of the observation in Equinox 2000.0<sup>b</sup> Exposure time after lightcurve screening (see §4.2)<sup>c</sup> Detector on the aim point

**Table 2.** Properties of the sample clusters. We show the redshifts, hydrogen column densities of the galactic absorption, temperatures, and X-ray fluxes of the sample clusters. The temperatures are referred to Reiprich & Böhringer (2002), Ota (2000), and Allen et al. (1996).

Cluster	redshift	$N_{\text{H}}^a$ [ $10^{20} \text{ cm}^{-2}$ ]	kT [keV]	$f_{\text{X}}^b$ [ $10^{-11} \text{ ergs s}^{-1} \text{ cm}^{-2}$ ]	Ref. <sup>c</sup>
A1060	0.0126	4.79	$3.24^{+0.06}_{-0.06}$	9.95	R
A133	0.0570	1.55	$3.80^{+2.00}_{-0.90}$	2.12	R
A1795	0.0622	1.20	$7.80^{+1.00}_{-1.00}$	6.27	R
A1835	0.2530	2.30	$7.42^{+0.61}_{-0.43}$	1.47	O
A2029	0.0780	3.07	$9.10^{+1.00}_{-1.00}$	6.94	R
A2052	0.0345	2.78	$3.03^{+0.04}_{-0.04}$	4.71	R
A2199	0.0310	0.87	$4.10^{+0.08}_{-0.08}$	10.64	R
A2204	0.1511	5.66	$7.21^{+0.25}_{-0.25}$	2.75	R
A2597	0.0822	2.50	$4.40^{+0.40}_{-0.70}$	2.21	R
A401	0.0748	10.3	$8.00^{+0.40}_{-0.40}$	5.28	R
A478	0.0881	14.8	$8.40^{+0.80}_{-1.40}$	5.15	R
A644	0.0704	6.95	$7.90^{+0.80}_{-0.80}$	4.02	R
A85	0.0557	3.37	$6.90^{+0.40}_{-0.40}$	7.43	R
A963	0.2057	1.40	$6.83^{+0.51}_{-0.51}$	0.59	O
AWM7	0.0172	9.91	$3.75^{+0.09}_{-0.09}$	1.58	R
Centaurus	0.0110	8.07	$3.68^{+0.06}_{-0.06}$	27.19	R
Hydra A	0.0538	4.90	$4.30^{+0.40}_{-0.40}$	4.78	R
MKW3S	0.0450	3.04	$3.70^{+0.20}_{-0.20}$	3.30	R
NGC5044	0.0089	5.03	$1.07^{+0.01}_{-0.01}$	5.51	R
PKS0745-191	0.1028	40.7	$7.21^{+0.11}_{-0.11}$	2.44	R
Sersic159-03	0.0580	1.76	$3.00^{+1.20}_{-0.70}$	2.49	R
ZW3146	0.2906	2.94	$6.10^{+0.30}_{-0.30}$	0.66	A
2A0335+096	0.0349	17.6	$3.01^{+0.07}_{-0.07}$	9.16	R

<sup>a</sup> Hydrogen column density of the galactic absorption.

<sup>b</sup> X-ray flux in units of  $10^{-11} \text{ ergs s}^{-1} \text{ cm}^{-2}$ . The energy bands are 0.1-2.4 keV for R and 2-10 keV for O and A.

<sup>c</sup> References R:Reiprich & Böhringer (2002), O:Ota (2000), and A:Allen et al. (1996).



**Table 3.** Fitting results of the temperature profiles with the exponential + constant model.

Cluster	$T_0$ [keV] <sup>a</sup>	$T_1$ [keV] <sup>a</sup>	$r_T^a$ [kpc]	$\chi_{\text{stat}}^2/\text{dof}^b$	Systematic error <sup>c</sup>
A1060	$3.16 \pm 0.22$	$-0.00 \pm 0.80$	$850.0 \pm 918.5$	126.4/4	0.183
A133	$4.52 \pm 0.36$	$-3.45 \pm 0.33$	$90.9 \pm 28.5$	20.7/4	0.082
A1795	$6.03 \pm 0.51$	$-3.36 \pm 0.57$	$151.4 \pm 63.1$	105.1/5	0.099
A1835	$10.10 \pm 0.69$	$-7.60 \pm 0.56$	$103.4 \pm 28.2$	10.2/4	..
A2029	$9.89 \pm 0.30$	$-5.73 \pm 0.34$	$144.4 \pm 22.7$	3.9/4	..
A2052	$3.20 \pm 0.27$	$-5.67 \pm 8.39$	$14.9 \pm 22.4$	24.8/2	0.734
A2199	$4.92 \pm 0.32$	$-3.34 \pm 0.41$	$57.2 \pm 22.2$	97.3/7	0.093
A2204	$8.45 \pm 1.29$	$-7.21 \pm 1.80$	$58.1 \pm 34.0$	26.1/3	0.235
A2597	$6.02 \pm 0.39$	$-4.33 \pm 0.35$	$162.7 \pm 29.1$	6.6/4	..
A401	$7.71 \pm 0.62$	$0.00 \pm 29.09$	$12.9 \pm 0.1$	19.0/2	0.170
A478	$7.03 \pm 0.35$	$-5.52 \pm 0.78$	$48.4 \pm 20.0$	33.6/6	0.076
A644	$6.47 \pm 0.39$	$-28.72 \pm 28.72$	$14.9 \pm 27.3$	27.6/3	0.128
A85	$6.44 \pm 0.27$	$-4.56 \pm 0.46$	$78.4 \pm 21.6$	26.0/5	0.065
A963	$6.22 \pm 0.25$	$-29.78 \pm 23.80$	$13.3 \pm 6.1$	1.5/2	..
AWM7	$3.78 \pm 0.10$	$-29.60 \pm 27.94$	$7.2 \pm 3.8$	52.8/4	0.064
Centaurus	$4.63 \pm 0.90$	$-3.92 \pm 0.86$	$78.0 \pm 35.2$	1167.4/7	0.215
Hydra A	$3.80 \pm 0.24$	$-0.95 \pm 0.28$	$113.3 \pm 95.0$	33.4/4	0.064
MKW3S	$3.71 \pm 0.14$	$-1.10 \pm 0.59$	$30.9 \pm 23.2$	42.3/7	0.078
NGC5044	$1.65 \pm 0.39$	$-1.10 \pm 0.37$	$102.9 \pm 54.5$	168.6/7	0.065
PKS0745-191	$11.16 \pm 0.65$	$-8.89 \pm 0.57$	$154.6 \pm 25.7$	9.9/3	..
Sersic159-03	$2.69 \pm 0.09$	$-1.31 \pm 0.13$	$58.0 \pm 15.7$	1.8/2	..
ZW3146	$8.04 \pm 0.31$	$-6.86 \pm 0.58$	$57.2 \pm 13.0$	0.6/2	..
2A0335+096	$3.96 \pm 0.40$	$-3.18 \pm 0.35$	$97.1 \pm 30.2$	60.6/4	0.089

<sup>a</sup> Errors are estimated by including a systematic error (see text).

<sup>b</sup> Original reduced  $\chi^2$  without a systematic error ( $\chi_{\text{stat}}^2$ ).

<sup>c</sup> Systematic error adopted so as to get the reduced  $\chi^2$  value of unity. This error includes the fluctuations in the intrinsic temperature profiles or unknown systematic errors in our analysis procedure.

**Table 4.** Fitting results of the gas density profiles with the NFW gas density model.

Cluster	$n_{e0}$ [ $10^{-2}$ cm $^{-3}$ ] <sup>a</sup>	$r_s$ [kpc] <sup>a</sup>	$B^a$	$\chi^2_{\text{stat}}/\text{dof}^b$	Systematic error <sup>c</sup>
A1060	0.83±0.09	145.1±48.2	5.13±1.08	565.3/4	0.078
A133	4.21±0.80	91.6±21.9	6.40±0.37	1584.3/4	0.121
A1795	4.76±0.45	252.8±37.6	8.54±0.50	6460.0/5	0.084
A1835	22.10±1.52	112.1±9.3	7.04±0.16	257.3/4	0.051
A2029	5.84±0.08	193.7±4.5	7.11±0.06	31.9/5	0.011
A2052	4.74±0.24	64.5±5.3	5.72±0.13	144.1/2	0.029
A2199	3.00±0.26	235.1±40.6	8.52±0.66	5112.0/7	0.079
A2204	21.60±3.10	89.3±14.4	7.15±0.28	557.3/3	0.10
A2597	8.11±0.62	157.4±17.6	8.94±0.38	537.9/4	0.071
A401	0.71±0.03	2842.0±664.9	19.05±10.64	97.6/2	0.035
A478	6.46±1.25	338.3±118.0	9.99±1.53	13901.8/6	0.155
A644	1.63±0.17	493.6±125.8	8.30±1.05	972.4/3	0.085
A85	3.86±0.48	122.5±21.6	5.76±0.26	2246.4/5	0.081
A963	2.76±0.13	477.2±58.5	9.07±0.57	39.3/2	0.033
AWM7	1.26±0.14	140.7±17.7	5.00±0.26	2899.1/4	0.083
Centaurus	7.79±1.75	24.7±5.5	5.72±0.23	6499.1/7	0.143
Hydra A	7.03±1.53	87.9±22.7	6.67±0.43	6555.0/4	0.151
MKW3S	3.23±0.33	106.7±20.5	5.95±0.41	608.8/7	0.083
NGC5044	3.98±0.95	34.8±15.5	6.22±0.95	3186.8/7	0.163
PKS0745-191	12.00±0.38	145.6±8.1	7.39±0.16	72.3/3	0.022
Sersic159-03	5.14±0.40	240.5±54.8	11.08±1.46	101.5/2	0.057
ZW3146	14.30±1.99	258.2±63.0	9.74±1.00	473.6/2	0.096
2A0335+096	9.23±1.30	90.5±17.3	7.41±0.47	1887.5/4	0.111

<sup>a</sup> Errors are estimated by including a systematic error (see text).<sup>b</sup> Reduced  $\chi^2$  without a systematic error ( $\chi^2_{\text{stat}}$ ).<sup>c</sup> Systematic error adopted so as to make the reduced  $\chi^2$  value unity.

**Table 5.** Fitting results of the mass profile with the general form of density profile given by Equation 12. The errors are 90 % confidence intervals.

Cluster	$r_s$ [kpc] <sup>a</sup>	$\alpha_0(0.02r_{200})$ <sup>a</sup>	$\chi^2_{\text{stat}}/\text{dof}$ <sup>b</sup>	Systematic error <sup>c</sup>
A1060	6.0±4.2	1.17±0.38	120.3/3	0.224
A133	1000 (fixed)	1.32±0.38	31.8/3	0.398
A1795	1000 (fixed)	1.29±0.43	194.2/4	0.482
A1835	51.1±200.1	0.82±0.47	13.9/3	0.278
A2029	760.0±1733.0	1.15±0.47	7.0/3	...
A2052	3.4±8.1	-0.14±0.96	176.4/1	0.524
A2199	163.3±8.2	0.64±0.46	36.8/6	0.440
A2204	1000 (fixed)	1.13±0.56	19.0/2	0.525
A2597	21.8±76.6	0.52±0.33	20.9/3	0.192
A478	3.1±3.5	0.17±0.42	23.8/4	0.308
A85	1000 (fixed)	0.94±0.37	95.6/4	0.365
AWM7	7.1±8.1	0.48±0.39	70.7/3	0.290
Centaurus	10.0±20.8	2.28±0.46	549.7/4	0.640
Hydra A	1000 (fixed)	1.85±0.55	237.3/3	0.556
MKW3S	86.4±101.8	1.22±0.18	17.1/4	...
NGC5044	1000 (fixed)	1.76±0.21	32.8/5	0.217
PKS0745-191	17.4±6.6	0.68±0.18	2.3/2	...
Sersic159-03	64.5±25.0	0.68±0.67	15.1/1	0.378
ZW3146	69.4±9.0	0.19±0.20	0.3/1	...
2A0335+096	15.4±35.3	0.56±0.10	11.9/3	...

<sup>a</sup> Errors are estimated by including a systematic error (see text).

<sup>b</sup> Reduced  $\chi^2$  before including a systematic error ( $\chi^2_{\text{stat}}$ ).

<sup>c</sup> Systematic error adopted so as to make the reduced  $\chi^2$  value unity.

**Table 6.** Remarkable structures in the central region of the sample clusters in literatures.

Cluster	Structure	Reference
A133	tongue	Fujita et al. (2002)
A1795	filament	Fabian et al. (2001)
A2052	holes	Blanton, Sarazin, McNamara, & Wise (2001)
A2199	depression	Johnstone, Allen, Fabian, & Sanders (2002)
A2597	cavities	McNamara et al. (2001)
Centaurus	plume	Sanders & Fabian (2002)
Hydra A	depression	McNamara et al. (2000)
NGC5044	hole	Buote, Lewis, Brighenti, & Mathews (2003)
MKW3S	filament & depression	Mazzotta et al. (2002)
2A0335+096	cavities & blobs	Mazzotta, Edge, & Markevitch (2003)

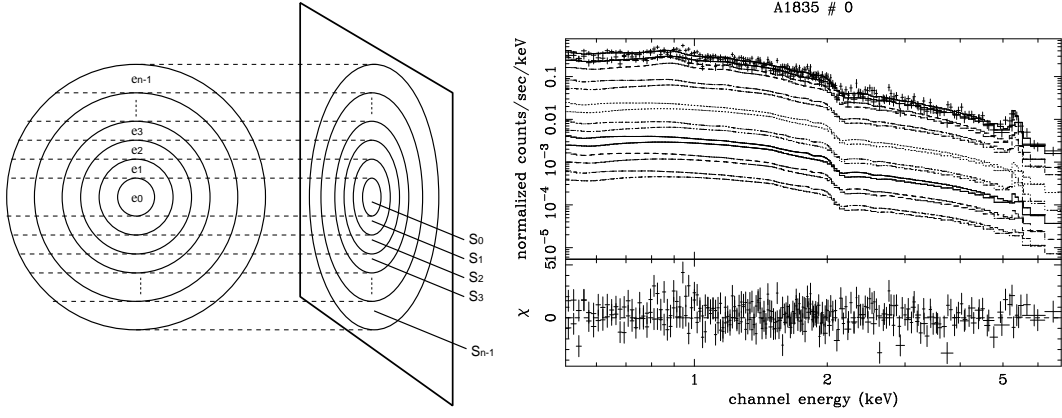


**Fig. 1.** (Left) Schematic view of the deprojection analysis. The left spheres represent X-ray emissions from  $N$  spherical shells, and the right circles represent observed projected luminosities which are the integrations of emissivities along the line of sight. (Right) An example of the spectrum fitting. In this example (A1835), we fitted the  $N = 7$  spectra for two data sets simultaneously. Observation IDs of each data set are 495 and 496.

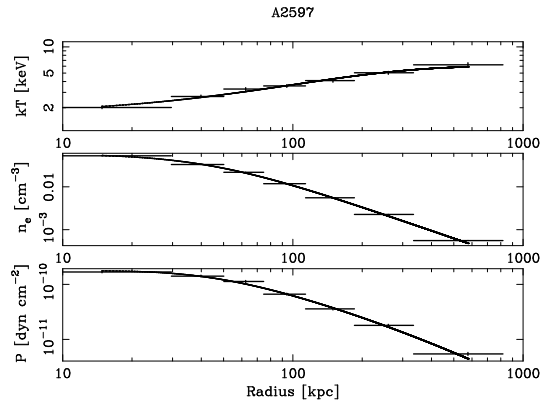


**Fig. 2.** The temperature, electron density, and pressure profiles of A2597. The solid lines represent best-fit models with analytical functions (Equation 4 and Equation 5). The pressure is simply derived from the temperature and gas density with the equation of state of the ideal gas:  $P = n_e kT$ .

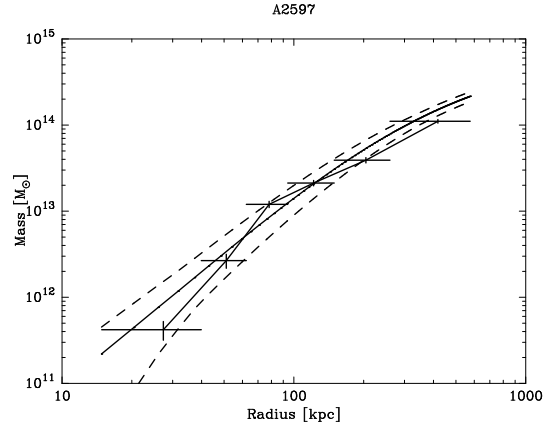


**Fig. 3.** The mass profiles of A2597. The solid curves represent the mass profile derived from the best-fit parameters of Equation 4 and Equation 5. The dashed lines are a confidence level of 68 %. The discrete data with error bars represent the mass profile calculated using approximate expression given by Equation 7.

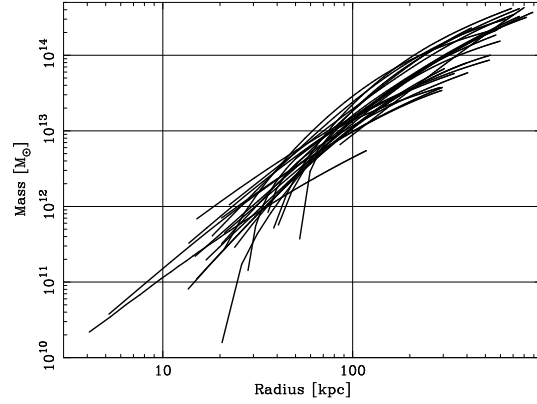


**Fig. 4.** Mass profiles of 23 sample clusters obtained from the temperature and density profile models.

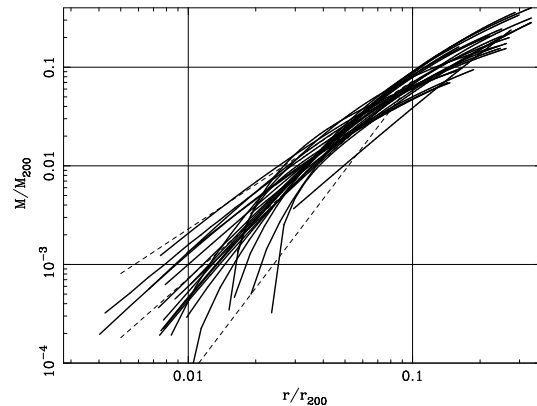


**Fig. 5.** Mass profiles scaled by  $M_{200}$  and  $r_{200}$ . For the calculation of  $r_{200}$  and  $M_{200}$ , we used the relation obtained from the numerical simulation by Evrard, Metzler, & Navarro (1996). The dashed lines represent  $M \propto r^{1.5}$  ( $\alpha = 1.5$ ),  $M \propto r^2$  ( $\alpha = 1$ ) and  $M \propto r^3$  ( $\alpha = 0$ ), respectively.

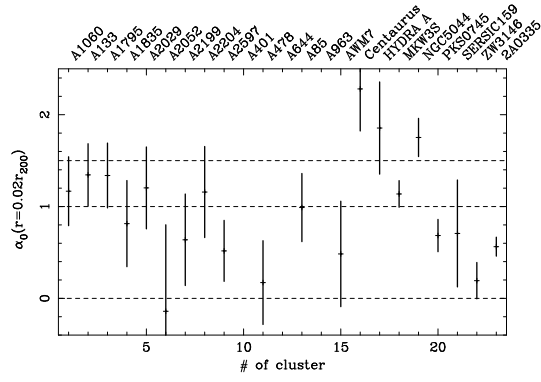


**Fig. 6.** Values of the Inner slope  $\alpha_0$  at the radius of  $0.02r_{200}$  for 20 clusters in Table 5. A401, A644, and A963 were removed due to a lack of data points within  $0.02r_{200}$ . The horizontal dashed lines represent  $\alpha = 1.5$  (Moore),  $\alpha = 1.0$  (NFW), and  $\alpha = 0.0$  (King). Error bars are shown at 90 % confidence level.

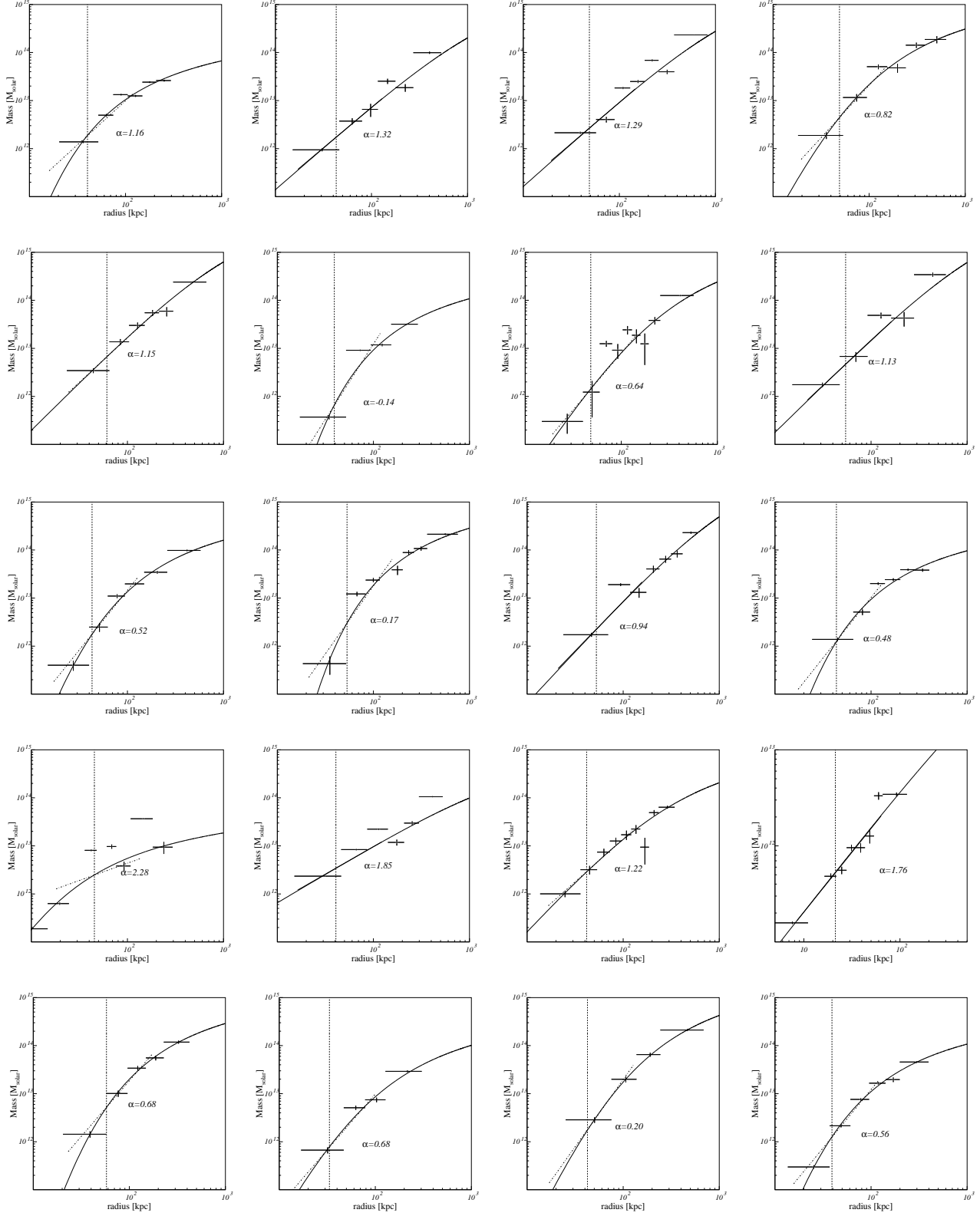


**Fig. 7.** The best-fit mass models using the general form of the density profile. The horizontal dashed lines represent the radius of  $r_0 = 0.02r_{200}$ . The dash-dotted lines represent the best-fit slope ( $M \propto r^{3-\alpha_0}$  at the radius  $r_0$ ). A401, A644, and A963 are removed because of the lack of the data within  $0.02r_{200}$ .



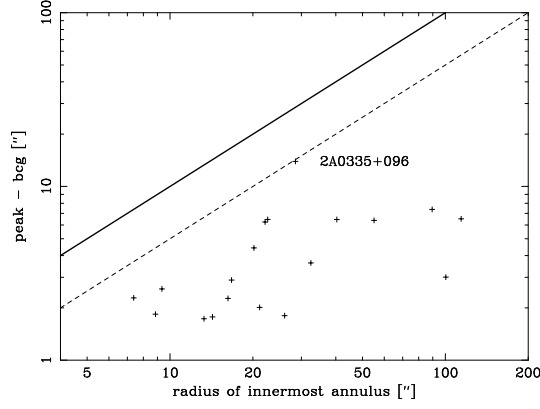


**Fig. 8.** Radius of the innermost annulus vs. offset between the X-ray peak and the BCG. The dashed line represents 50 % of the radius of the innermost annulus.

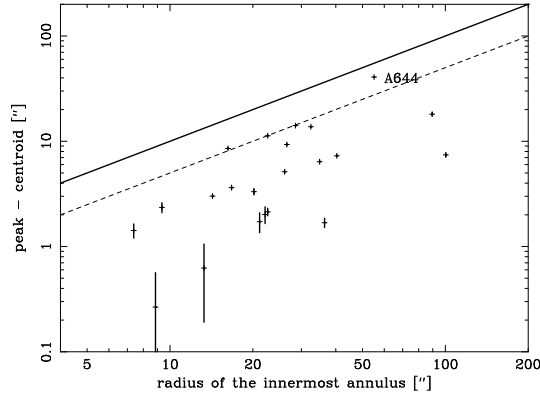


**Fig. 9.** Radius of the innermost annulus vs. offset between the X-ray peak and the X-ray centroid. The dashed line represents 50 % of the radius of the innermost annulus.

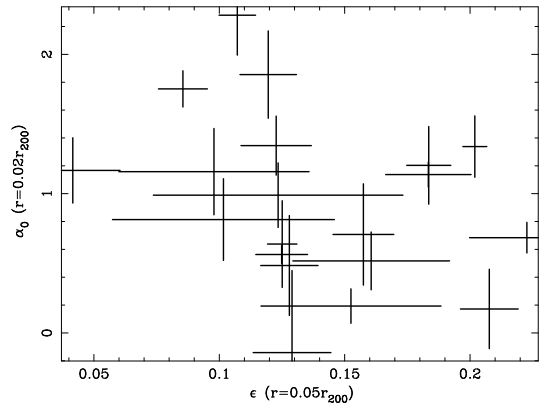


**Fig. 10.** Ellipticity  $\epsilon$  vs. inner slope  $\alpha_0$ . The errors are  $1\sigma$  (68.3 %) confidence level. The correlation coefficient is  $-0.31$  for this relation.

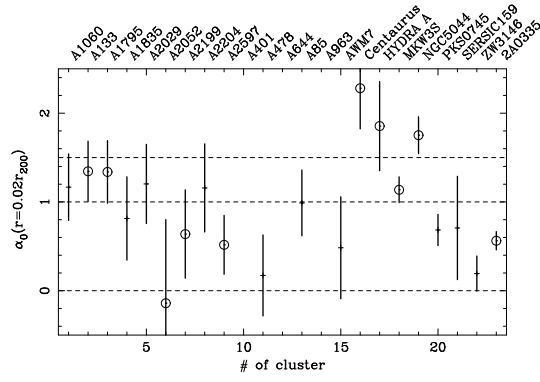


**Fig. 11.** Inner slope  $\alpha_0$  of mass profiles. The circles indicate 10 clusters in the literatures to have the central structure (see Table 6).

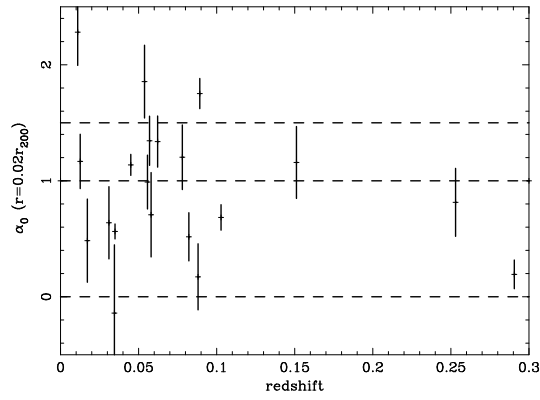


**Fig. 12.** Redshift vs. inner slope  $\alpha_0$ . The correlation coefficient is -0.25 for this relation.

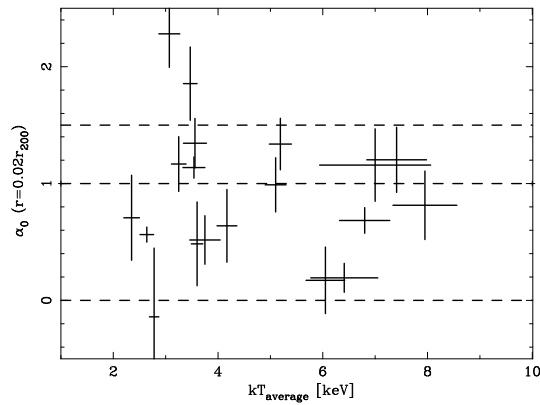


**Fig. 13.** Temperature vs. inner slope  $\alpha_0$ . The correlation coefficient is 0.01 for this relation.

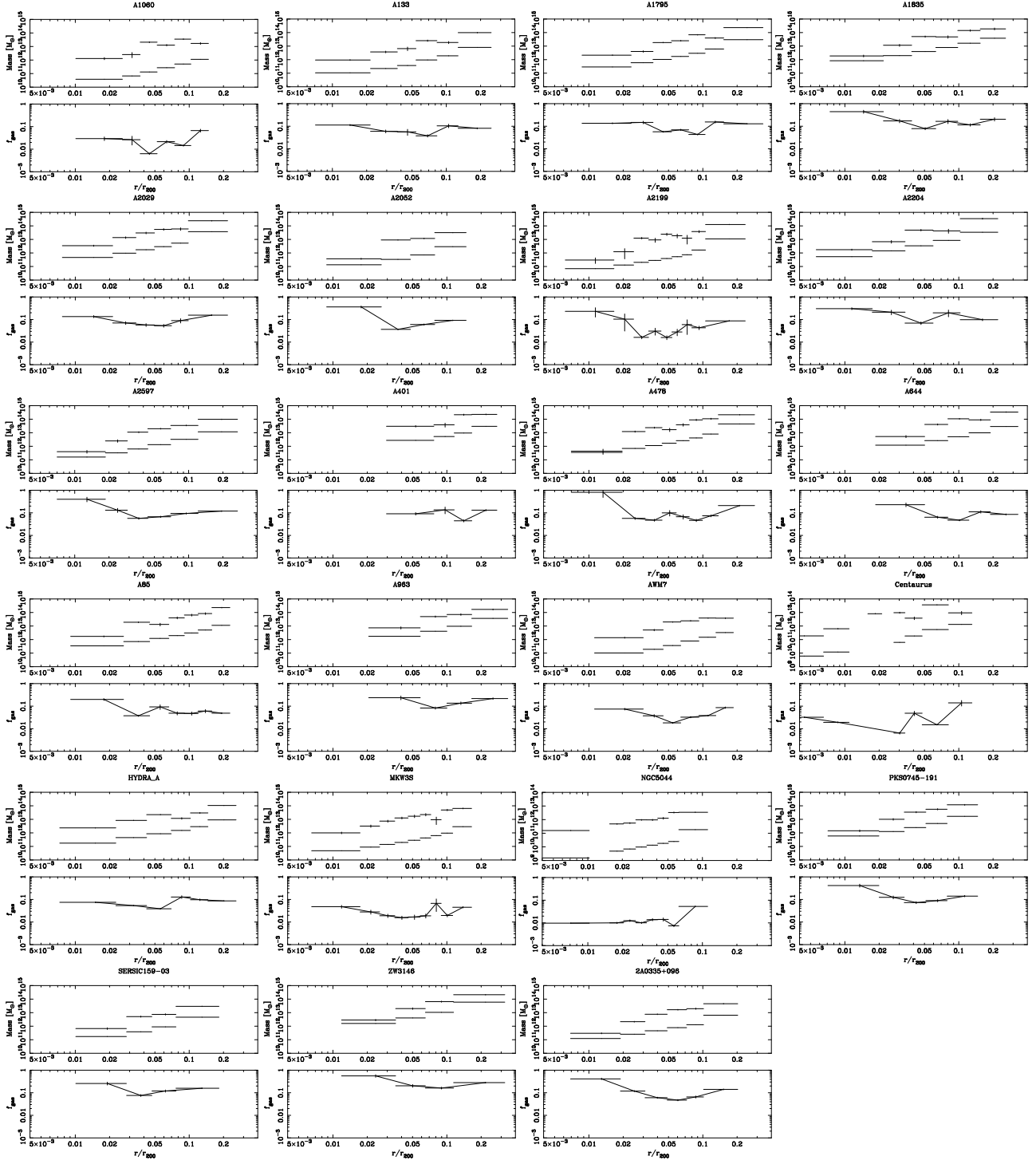


**Fig. 14.** Total integrated mass, gas mass, and gas fraction profiles of the 23 sample clusters. The radius is scaled with  $r_{200}$ . We show the total integrated mass and gas mass profiles in the upper panel, and the gas fraction profile in lower panel.

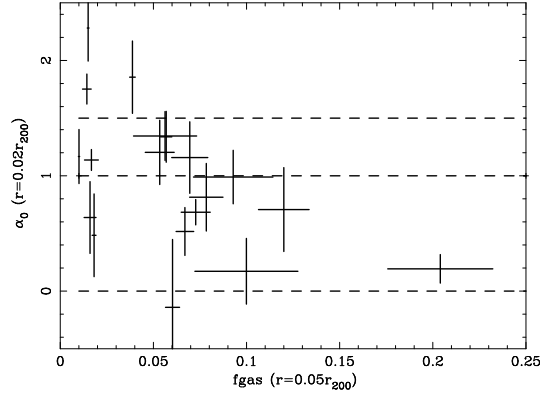


**Fig. 15.** Gas fraction at the radius of  $r = 0.05r_{200}$  vs. inner slope  $\alpha_0$ . The correlation coefficient is  $-0.51$  for this relation.

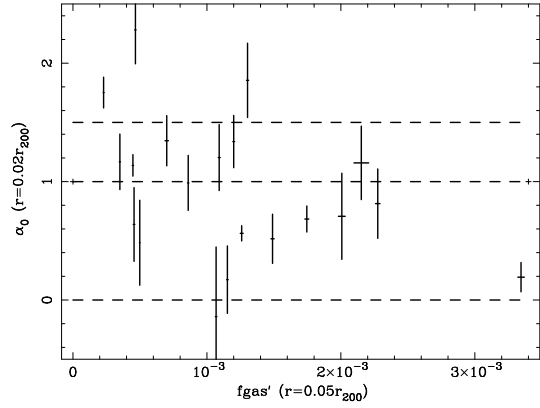


**Fig. 16.** Gas fraction redefined in Equation 21 ( $f'_{\text{gas}}$ ) vs. inner slope  $\alpha_0$ . The correlation coefficient is  $-0.40$  for this relation.

## References

- Allen, S. W., Fabian, A. C., Edge, A. C., Bautz, M. W., Furuzawa, A., & Tawara, Y. 1996, MNRAS, 283, 263
- Arabadjic, J. S., Bautz, M. W., & Garmire, G. P. 2002, ApJ, 572, 66
- Blanton, E. L., Sarazin, C. L., McNamara, B. R., & Wise, M. W. 2001, ApJL, 558, L15
- Blumenthal, G. R., Faber, S. M., Flores, R., & Primack, J. R. 1986, ApJ, 301, 27
- Buote, D. A., Lewis, A. D., Brighenti, F., & Mathews, W. G. 2003, ApJ, 594, 741
- Carter, D. & Metcalfe, N. 1980, MNRAS, 191, 325
- David, L. P., Nulsen, P. E. J., McNamara, B. R., Forman, W., Jones, C., Ponman, T., Robertson, B., & Wise, M. 2001, ApJ, 557, 546
- El-Zant, A., Shlosman, I., & Hoffman, Y. 2001, ApJ, 560, 636
- Ettori, S., Fabian, A. C., Allen, S. W., & Johnstone, R. M. 2002, MNRAS, 331, 635
- Evrard, A. E., Metzler, C. A., & Navarro, J. F. 1996, ApJ, 469, 494
- Fabian, A. C., Sanders, J. S., Ettori, S., Taylor, G. B., Allen, S. W., Crawford, C. S., Iwasawa, K., & Johnstone, R. M. 2001, MNRAS, 321, L33
- Firmani, C., D'Onghia, E., Chincarini, G., Hernández, X., & Avila-Reese, V. 2001, MNRAS, 321, 713
- Fujita, Y., Sarazin, C. L., Kempner, J. C., Rudnick, L., Slee, O. B., Roy, A. L., Andernach, H., & Ehle, M. 2002, ApJ, 575, 764
- Henriksen, M. J. & Markevitch, M. L. 1996, ApJL, 466, L79
- Johnstone, R. M., Allen, S. W., Fabian, A. C., & Sanders, J. S. 2002, MNRAS, 336, 299
- Kaastra, J. S. & Mewe, R. 1993, A&AS, 97, 443
- Katayama, H. 2003, PhD thesis, Osaka University
- Liedahl, D. A., Osterheld, A. L., & Goldstein, W. H. 1995, ApJL, 438, L115
- Makino, N., Sasaki, S., & Suto, Y. 1998, ApJ, 497, 555
- Mazzotta, P., Kaastra, J. S., Paerels, F. B., Ferrigno, C., Colafrancesco, S., Mewe, R., & Forman, W. R. 2002, ApJL, 567, L37
- Mazzotta, P., Edge, A., & Markevitch, M. 2003, ApJ, 596, 190
- McNamara, B. R. et al. 2000, ApJL, 534, L135
- McNamara, B. R. et al. 2001, ApJL, 562, L149
- Mewe, R., Gronenschild, E. H. B. M., & van den Oord, G. H. J. 1985, A&AS, 62, 197
- Mewe, R., Lemen, J. R., & van den Oord, G. H. J. 1986, A&AS, 65, 511
- Moore, B., Governato, F., Quinn, T., Stadel, J., & Lake, G. 1998, ApJL, 499, L5
- Navarro, J. F., Frenk, C. S., & White, S. D. M. 1995, MNRAS, 275, 56
- Navarro, J. F., Frenk, C. S., & White, S. D. M. 1996, ApJ, 462, 563
- Navarro, J. F., Frenk, C. S., & White, S. D. M. 1997, ApJ, 490, 493
- Ota, N. 2000, PhD thesis, University of Tokyo
- Reiprich, T. H. & Böhringer, H. 2002, ApJ, 567, 716
- Sand, D. J., Treu, T., & Ellis, R. S. 2002, ApJL, 574, L129
- Sanders, J. S. & Fabian, A. C. 2002, MNRAS, 331, 273
- Swaters, R. A., Madore, B. F., van den Bosch, F. C., & Balcells, M. 2003, ApJ, 583, 732
- Voges, W. et al. 1999, A&A, 349, 389